A deformation twin mediated consecutive sliding-opening crack propagation mechanism leading to zig-zag fracture in multi-principal element alloys

Qi Zhu[1,#], Zhi Li[2,#], Siyuan Wei[3], Yakai Zhao[3], Upadrasta Ramamurty[1], Jiangwei Wang[4], Huajian Gao[1,5,*]

[1]School of Mechanical and Aerospace Engineering, College of Engineering, Nanyang Technological University, Singapore 639798, Republic of Singapore

[2]Institute of High Performance Computing (IHPC), Agency for Science, Technology and Research (A*STAR), Singapore 138632, Republic of Singapore

[3]Institute of Materials Research and Engineering (IMRE), Agency for Science, Technology and Research (A*STAR), Singapore 138634, Republic of Singapore

[4]Center of Electron Microscopy and State Key Laboratory of Silicon and Advanced Semiconductor Materials, School of Materials Science and Engineering, Zhejiang University, Hangzhou 310027, China

[5]Mechano-X Institute, Applied Mechanics Laboratory, Department of Engineering Mechanics, Tsinghua University, Beijing 100084, China

[#]These authors contributed equally: Qi Zhu, Zhi Li

*To whom correspondence may be addressed.

Email gao.huajian@mail.tsinghua.edu.cn

Abstract

Multi-principal element alloys (MPEA) have emerged as a class of high-performance materials. Of particular interest is the excellent fracture toughness in face-centered cubic MPEAs with low stacking fault energy, where abundant deformation twins are commonly observed. To understand the fracture mechanism in such MPEAs, here we perform in situ nanomechanical testing inside transmission electron microscope, atomistic simulation, and theoretical analysis to investigate the mechanism of interaction between a propagating crack and a coherent twin boundary (TB) in CoCrFeNi MPEA. We unveil a hitherto unknown microscopic mechanism of crack-TB interaction in MPEAs, where sliding along secondary nanotwins (NTs) nucleated from the primary TB followed by daughter crack nucleation some distance ahead of the main crack constitute a consecutive sliding-opening crack propagation mechanism, leading to zig-zag fracture around the primary TB. The origin of this mechanism lies in the frequent nucleation of NTs from steps on the primary TB, which can effectively blunt and deflect a propagating crack. Quantitative analysis indicates nearly doubled fracture resistance associated with this unique mechanism of crack-TB interaction in MPEAs. These findings bring about a missing aspect in TB-modulated fracture in MPEAs and enrich our understanding of the enhanced damage tolerance of alloys with low stacking fault energy.

Key words: Twin boundary, crack propagation, fracture, multi-principal element alloy

1. Introduction

Multi-principal element alloys (MPEAs) have emerged as a class of structural materials that offer a wide range of exceptional mechanical properties through the exploitation of all the available alloy design principles [1-5]. Of particular interest is the excellent damage tolerance that are commonly observed in face-centered cubic (FCC) MPEAs, such as the equiatomic CoCrFeNiMn (widely referred to as the 'Cantor alloy') [6, 7], at both room and cryogenic temperatures. Through the manipulation of compositions, the plastic deformation mechanisms in them can be further modified, giving rise to the emergence of new alloys such as CoCrFeNi [8, 9] and CoCrNi [10-12]. These alloys demonstrate excellent mode I fracture toughness (J_{Ic}) that exceeds 200 kJ/m^2 [13], which can even further increase at cryogenic temperature. Such exceptional fracture toughness in this class of FCC MPEAs is generally attributed to the twinning-dominated deformation mechanism [14, 15], which is facilitated by their characteristic low stacking fault energy (SFE) [16]. In addition, the low SFE also introduces numerous annealing twins in MPEAs during fabrication and processing, which also affect subsequent deformation behaviors and damage tolerance [17-19].

In spite of the widely acknowledged conclusion of twinning enhanced toughness in FCC MPEA, an outstanding gap remains in our understanding of the roles and underlying mechanisms of twins and their impact on both intrinsic and extrinsic toughness [20]. The intricate interactions between twin boundaries (TBs) and propagating cracks impose considerable challenges in accurately delineating the underlying mechanisms during the fracture process. On the one hand, extensive deformation twins requires a threshold activation stress and hence commonly occur at the latter stages of deformation at room temperature [21]; on the other hand, certain conditions can facilitate twinning-dominated deformation, such as at cryogenic temperature [22] or high strain rate [23]. Complex microstructures and stress states often render it difficult to precisely trace the interactions between twins and cracks. In addition,

secondary or high order nanotwins (NTs) are commonly observed in FCC alloys with low SFE [24, 25], as inherent TB defects (*e.g.*, steps) facilitate the nucleation of secondary twins [26, 27], which further enhances the fracture energy [28]. These complex twin architectures add another degree of challenge to interpreting the TB-crack interaction, especially to decoupling the contributions of each twinning system to the overall fracture toughness, which is beyond the capability of simple post-mortem microstructural analysis. While in situ microscale fracture test using scanning electron microscopy (SEM) is a promising method to simultaneously uncover the extensive twinning behaviors ahead of the crack tip and determine the fracture toughness [29], it can hardly distinguish the nanoscale or atomic-scale structural evolution and decouple the contribution from each individual TB-crack interaction mode. Molecular dynamics (MD) simulations, on the other hand, have been widely used to reveal the atomistic mechanism underlying TB-induced toughening by investigating the interactions involving crack tip, dislocations, and TBs in representative FCC metals and alloys [30-32]. However, most existing studies have been limited to simplified microstructures and idealized TB structures, while mechanistic insight in twinning-enhanced fracture resistance remains scarce, especially for MPEAs with complex twin structures.

Keeping the above in view, we take CoCrFeNi, a typical single-phase FCC equiatomic MPEA with SFE of ~20 mJ/m^2 [17], here as the model material to elucidate the dynamic interplay between a propagating crack and a primary TB, via a combination of in situ nanomechanical testing inside transmission electron microscope (TEM), MD simulations, and theoretical analysis. In situ observations reveal a consecutive sliding-opening crack propagation mechanism via sliding along secondary nanotwins (NTs) nucleated from the primary TB followed by daughter crack nucleation some distance ahead of the main crack, which lead to a microscopically zig-zag crack propagation in the vicinity of TB. MD simulations help clarify the deformation mechanisms leading to the observed zig-zag crack

path, including coordinated dislocation pile-ups, NT sliding and sub-crack nucleation between neighboring secondary NTs. Theoretical analysis based on surface energy and TB sliding energy considerations quantitatively elaborates the enhanced fracture resistance associated with the zig-zag crack propagation, which is confirmed by the crack tip opening displacement (CTOD) measured in experiment. These findings provide a detailed understanding of the TB-modulated fracture in FCC MPEA, when combined with classic models may help guide the design of high-performance alloys through defect engineering.

2. Experiments and simulations

2.1 Sample preparation

$Co_{25}Cr_{25}Fe_{25}Ni_{25}$ (in at.%) equiatomic MPEA ingots with single FCC phase were fabricated by vacuum induction melting of the four constituent elements (purity ≥99.9 wt.%) and drop casting. The as-cast samples were sequentially hot-rolled at 1050 °C to a 64% thickness reduction, homogenized at 1100 °C for 1 h, cold-rolled to a further 60% thickness reduction, and, finally, annealed at 1100 °C for 1 h. The samples for further characterization and in situ testing were cut from the original ingot, followed by mechanical grinding with SiC abrasive paper and then polished using 0.04 μm colloidal silica suspension (Struers). The grain morphologies and the corresponding crystallographic orientation maps were obtained using scanning electron microscope (SEM, JEOL JSM-7800F Prime) equipped with an Aztec symmetric electron backscatter diffraction (EBSD) detector. Fig. 1a shows the typical grain morphology of the as-annealed coarse-grained CoCrFeNi MPEA with an average grain size ~40 μm, where the superimposed inverse pole figure (IPF-Z) confirms the frequent presence of annealing twins and concurrent Σ3 coherent TBs. Based on the IPF-Z orientation map, $[11\bar{2}]$-aligned annealing twins (or their vicinal orientation) were selected for fabricating twinned crystal (TC) specimens, each of which contain an edge-on coherent TB parallel to the

indentation direction. For comparison, [11$\bar{2}$]-aligned single crystal (SC) specimens were also fabricated within the grain near the selected TB.

2.2 Site-selective specimen fabrication

Microscale fracture test specimens for in situ TEM were fabricated using focused ion beam (FIB, Zeiss Crossbeam 540). Cross-sectional lamellae (with a thickness of approximately 1.5 μm) with a TB in the middle were first lifted out of the selected regions in the bulk sample according to EBSD orientation map, using an Omiprobe manipulator. The height and thickness of the lifted lamella align along the [11$\bar{2}$] and [1$\bar{1}$0] directions, respectively. The lamella was then transferred and attached to a Mo grid, followed by patterning of fracture test specimens using Ga^+ ion beam (30 kV, 1.5 nA). The fine milling process of the electron-transparent film region in the middle of each specimen was completed under sequential ion beam currents of 300, 100, and 20 pA (see Supplementary Fig. 1). A notch with an average width below 200 nm was cut on top of the film with a low current of 2 pA, which ensures the activation of a sharp crack from the notch surface. A low voltage polishing (5 kV, 10 pA) was performed to eliminate potential amorphous layers on both sides. Fig. 1b shows a typical FIB-fabricated microscale fracture test specimen, which contains a uniform electron transparent film in the middle. The width and thickness of the film are approximately 2 μm and 100 nm, respectively.

2.3 In situ nanomechanical testing and microstructural characterization

In situ nanomechanical testing were performed using X-Nano holder (developed by the Center for X-Mechanics of Zhejiang University [33]) in double aberration-corrected TEM (JEOL JEM-ARM300F) operating at 300 kV. Before in situ fracture test, the specimens (attached on Mo grid) and W indenter were installed on the static and mobile sides in the loading module of the holder, respectively. During the in situ test inside TEM, the W indenter

(with a half-angle of approximately 60°) was actuated by a piezo controller to move towards the specimen (Fig. 1c). Nanoindentation was conducted under displacement control mode with an approximate rate of 5 nm/s. Through the push-to-pull specimen design, conventional nanoindentation was converted to microscale fracture test of the film, where the crack was initiated from the notch surface. After the in situ microscale fracture test, microstructural characterization along the crack was conducted with both high-resolution TEM and high-angle annular dark field scanning transmission electron microscopy (HAADF-STEM) with a semi-convergence angle of approximately 28 mrad and a dwell time of 8 s.

2.4 Atomistic simulations

MD simulations were performed using the large-scale atomic/molecular massively parallel simulator (LAMMPS) [34] with embedded-atom method (EAM) interatomic potentials for random equiatomic CoCrFeNi alloys [35]. The dimensions of the typical model for crack propagation simulation were set at around $60\times50\times3$ nm^3, which contains approximately 0.8×10^6 atoms each. Solid solution CoCrFeNi samples were created by randomly replacing three-quarters of the Ni atoms in an FCC Ni sample with equal number of Co, Cr and Fe atoms. Secondary NTs with different thicknesses were introduced between the primary TBs, where atomic steps with different heights were created to mimic the initial distribution of defects on the secondary TBs. An atomically sharp crack was created by removing one layer of atoms on the inclined $(\bar{1}11)$ plane and screening the corresponding interaction of atoms across the crack interface. The whole system was annealed at 5 K for 300 ps for energy minimization. Displacement-controlled loading was then applied to the model along X-[111] direction (perpendicular to the primary TB) at an engineering strain rate of $\sim6.5\times10^7$ s^{-1}. Periodic boundary condition was adopted along X-[111] direction, while free surface condition was adopted in Y-$[11\bar{2}]$ and Z-$[1\bar{1}0]$ directions, respectively. The open access tool Ovito [36] was

used to visualize and analyze the simulation results, where common neighbor analysis (CNA) was applied to delineate the crack surface and TBs from the FCC matrix.

To evaluate the TB sliding energy, a 20×20×20 nm^3 equiatomic CoCrFeNi alloys bulk sample was created, which contains a single TB in the middle. Periodic boundary conditions were adopted in the X-[$1\bar{1}0$] and Y-[$11\bar{2}$] directions, while the free surface condition was adopted in the Z-[111] direction. The upper half of the sample above the TB was shifted along the [$1\bar{1}0$] direction and the stress-displacement curve was derived from the total energy with respect to displacement. The TB sliding energy for a unit length (b=1/2[$1\bar{1}0$]) was thus obtained by integrating the positive part of the stress-displacement curve along the sliding direction.

3. Results

3.1 Consecutive crack deflection in the vicinity of a pre-existing TB

At the beginning of microscale fracture test, shear localization along the ($\bar{1}11$) or ($1\bar{1}1$) close-packed planes, which are inclined through the specimen thickness, preferentially occur from the surface of pre-set notch in the [$11\bar{2}$]-aligned specimen (Fig. 1d). The shear localization arises from the preferential nucleation of full dislocations with a Burgers vector of 1/2[110] and a Schmid factor of 0.272. The solid and dashed lines delineate the intersections of this inclined plane with the top and bottom surfaces of the specimen, respectively. Since the consecutively activated dislocations contain a Burgers vector component parallel to the film thickness, the associated shear localization inevitably induces rapid mechanical thinning, which eventually generates a sharp crack along this close-packed plane. Adopting this controlled crack-generating method to TC specimens (containing an individual coherent TB in the film), we can directly investigate the interaction between individual TB and a propagating crack in the CoCrFeNi MPEA, as shown by the snapshots in Fig. 2. First, the crack propagates towards the pre-existing TB (with a slant angle of ~5° with respect to the indentation direction),

which is blocked instantly and deflected onto the TB (see Fig. 2a and schematic in Fig. 2c). With further loading, the main crack is deflected again by a secondary NT, which is generated from the primary TB ahead of the crack (Fig. 2b and schematic in Fig. 2d), instead of propagating along the TB. After the blunting of this main crack by the secondary NT, a new sub-crack is generated ahead of this NT following the shear localization path parallel to the main crack. This new sub-crack then merges with the NT-blunted main crack, which appears to deflect the main crack back to the primary TB. With continued loading, such consecutive crack deflections by the secondary NTs and the re-activation of sub-crack ahead proceed in a periodic manner, leading to a zig-zag mode of crack propagation in the vicinity of the primary TB (Fig. 2e), even after crack transits across the primary TB into the neighboring grain.

Multiscale structural characterizations were conducted to further elaborate this zig-zag crack behavior in the vicinity of the primary TB in terms of consecutive crack blunting and deflection processes. High-resolution TEM image (Fig. 3a) shows that the first blunting of the main crack arises from the pre-existing coherent TB ahead, which deflects the crack to TB. Meanwhile, several steps and stacking faults (SFs) are generated from this TB segment near the blunting site of the crack, indicating significant plastic deformation (for mitigating the stress concentration) during this crack deflection process. Fig. 3b shows that the subsequent crack deflection is induced by the secondary NT activated from a large step in the inherently defective TB, which is confirmed by the corresponding fast Fourier transform (FFT) pattern in Fig. 3e. It has been previously shown that the nucleation of secondary NTs can effectively mitigate the stress concentration at large TB steps in FCC metals [26]. Here, the atomic structure of the large TB step (with 20 atom layers) resulting from this energy release route is unveiled by HAADF-STEM (Fig. 3f), which exhibit an asymmetrical interface configuration towards the Σ9 GB. In contrast, a smaller TB step (with 9 atom layers) that is nearby only favors the nucleation of a partial dislocation bound by an SF, while retaining an ideal incoherent

TB configuration (Fig. 3g). Most importantly, the activation of a secondary NT ahead of the main crack impedes potential cleavage along the primary TB. Instead, the crack is deflected onto the secondary NT, inducing sliding along NT. However, such sliding is limited by the length of the secondary NT, where further lattice sliding ahead is dominated by SFs near the surface (Fig. 3c). The accumulated shear offset inevitably introduces structural instability, which can impair continued deformation via TB sliding [37, 38]. A new sub-crack arising from the preferential inclined slip is generated some distance ahead of the NT, which then merges with the main crack (Fig. 3d), leading to the apparent crack deflection back to the primary TB. With further loading, consecutive crack deflections induced by the frequent activation of secondary NTs can proceed periodically in the vicinity of the inherently defective TB, leading to the zig-zag crack growth (Fig. 2e). A similar zig-zag crack pattern in the vicinity of primary TB is shown in Supplementary Fig. 2.

3.2 Sliding-opening mechanism leading to zig-zag crack

According to the crystallographic relations of the four equivalent {111} slip planes in FCC metals with respect to the direction of indentation, the inclined crack along $(1\,\bar{1}\,1)$ plane generated from the notch can either propagate towards (Fig. 2) or away from a pre-existing TB in the specimen. Fig. 4 shows that a similar zig-zag mode of cracking can also be activated when the main crack propagates away from the TB. As shown in Fig. 4a, the main crack along the inclined slip plane initially propagates away from the slanted TB (oriented at an angle of approximately 12° with respect to the indentation direction). Meanwhile, secondary NTs (denoted as NT1 to NT3) are generated from the primary TB, which instantly blunt the main crack. After blunting, the stress concentration near the crack tip continues to accumulate, which can be seen from the contrast change in dark-field TEM snapshot. With the activation of localized shear on the other side of NT1, the stress concentration at the crack tip is effectively

released (Fig. 4b). Similar to that shown in Fig. 3, this shear localization is coordinated with TB sliding along NT1 at the crack blunt region, which activates the nucleation of a sub-crack that rapidly propagates towards NT2 (Fig. 4b). In this way, the crack tip proceeds ahead to NT2 through a zig-zag propagation route, which is similar to that shown in Fig. 2. The blunting of sub-crack 1 that follows then catalyzes the same consecutive crack blunting and nucleation of sub-crack 2 between NT2 and NT3 (Fig. 4c), leading to a periodic zig-zag crack pattern in the vicinity of the primary TB. These results also indicate that the zig-zag crack can occur in a range of TB orientations, given the preferential activation of secondary NTs in the CoCrFeNi MPEA.

In addition to individual TBs, similar zig-zag crack growth was also observed along the hierarchical NT structures in the CoCrFeNi MPEA specimen. As shown in Fig. 4d, a primary NT parallel to the indentation direction (with a thickness of approximately 7 nm at the notch root and reduces to several atomic layers in the front) pre-exists in a $[11\bar{2}]$-aligned specimen. During the fracture test, the main crack nucleates from the notch root and propagates away from the pre-existing NT; meanwhile, multiple secondary NTs (denoted as NT1 and NT2) are activated from the primary NT, generating a hierarchical NT configuration. Similar to that shown in Fig. 4a, the propagating crack is instantly blunted at NT1, followed by the activation of inclined slip from NT1 to NT2 (Fig. 4e, shown by the white arrow). With continuous sliding along NT1 ahead of the blunted crack tip under further loading, shear localization along this slip plane between NT1 and NT2 evolves into a sub-crack (Fig. 4f). Therefore, zig-zag crack propagation can also be induced upon its interaction with the hierarchical NT configurations. In contrast, in $[11\bar{2}]$-aligned SC specimen without the hierarchical NT structures, the crack keeps propagating rapidly along the inclined $(\bar{1}11)$ plane without any deflection (Fig. 4g–i). The above comparison among TC, hierarchical NTs, and SC specimens underpins the indispensable role of secondary NTs in activating zig-zag crack in the vicinity of inherently

defective TBs and modulating the overall crack propagation resistance of CoCrFeNi, a typical MPEA alloy with relatively low SFE.

To further understand the origin of this zig-zag crack propagation, MD simulations have been performed to unravel the atomistic mechanisms underlying the interaction between a crack and secondary NTs. As shown in Fig. 5a, the initial model adopts the same $[11\bar{2}]$-aligned TC configuration as that in experiment (Fig. 4), where the main crack along the inclined $(1\bar{1}1)$ plane is initially blunted by NT1 that nucleated from the primary TB. Under tensile loading perpendicular to the primary TB plane, TB sliding along the NT is preferentially activated through the consecutive activation of full dislocations (presented as leading and trailing partial dislocation pairs) from the blunted crack tip with evident stress concentration (see the atomistic distribution of von-Mises strain in Fig. 5d). The dislocations propagating along the NT pile-up at pre-existing atomic steps, which induces local stress concentration that leads to dislocation nucleation from the opposite side of NT1 (Figs. 5b and 5e). The inclined slip ahead of NT is activated due to steps on the boundary of secondary NTs. These steps on the secondary TBs play an essential role in creating the local concentrated plastic deformation on the TBs by blocking the twinning dislocation pairs emitted from the crack tip and creating dislocation pile-up. The corresponding local stress concentration at the steps serve as nucleation sites to re-activate the slips ahead, which coordinates with sliding along the secondary NT. With further tensile loading, inclined slip systems can be activated at the intersection of the primary and secondary TBs (Fig. 5c) and propagate towards the neighbouring TBs. This mechanism serves as the transfer route of plastic deformation between different TBs along the crack path. Consistent with our experimental observations, these inclined slip systems have disassociated Burgers vectors along the thickness direction and inevitably induce local mechanical thinning of the sample, which leads to the formation of a sub-crack connecting the neighboring secondary NTs. The evolution of atomistic von Mises strain (Fig. 5f) delineates strong strain

accumulation along the secondary NT, which confirms the transfer of plastic deformation among the secondary TBs ahead of the crack tip during the zig-zag crack propagation. Atomistic characterization of the TB sliding region through HRTEM near the nucleation site of sub-crack ahead also shows frequent presence of atomic steps in the secondary NTs (Supplementary Fig. 3), which serve to restrict TB sliding along the secondary NTs, supporting our MD simulations results. Meanwhile, these steps on the TB can also serve as effective nucleation sites of full dislocations on the inclined slip plane, contributing to the re-activation of inclined sub-crack ahead. These observations confirm the important role of steps in the secondary NT, which highlights a new role of TBs in modulating the fracture behaviour in the presence of multiple secondary NTs.

3.3 Enhanced fracture resistance with zig-zag crack propagation

To quantitatively estimate the enhanced fracture resistance associated with the observed zig-zag crack, the crack tip opening displacement (CTOD) coupled with crack propagation distance (L) projected along the indentation direction has been recorded. Fig. 6a–b schematically illustrates the CTOD and L in normal crack and zig-zag crack, where the same L from the pre-set notch is assumed in both models for comparison. The ratios between CTOD and L are determined for both normal and zig-zag cracks among parallel specimens in experiments (Table 1). For the normal crack, *i.e.*, direct crack propagation along the inclined $(1\bar{1}1)$ slip plane, the CTOD/L ratio in the range of 0.21–0.28 has been determined from multiple specimens. In contrast, the CTOD/L ratio for zig-zag crack increases markedly to above 0.36 (with a maximum value of approximately 0.48), indicating at least 50% increase in fracture resistance due to crack deflection. Essentially, the increased resistance against crack propagation can be attributed to three major factors associated with the secondary NT, including: (1) crack blunting by NT; (2) transition from cracking along the inclined $(1\bar{1}1)$ plane

to sliding along the secondary NT; (3) nucleation of sub-crack ahead following the extensive dislocation motion along the inclined plane, which is coordinated with sliding along the NT.

While the apparent blunting of main crack by the secondary NT has been observed in both experiments (Fig. 4) and MD simulations (Fig. 5), the latter two processes require further clarification. Step-by-step analysis of such NT-modulated fracture behaviour in the CoCrFeNi MPEA specimen establishes a correlation between the TB sliding distance and the nucleation of a sub-crack ahead during the zig-zag crack propagation. As shown in Fig. 7a–b, the continuous crack opening following the crack blunting is mainly induced by the sliding along secondary NT. During this process, the displacement associated with sliding along the NT inevitably induces stress concentration at steps on the NT, which is preferentially released through consecutive dislocation motion along the inclined slip between the neighboring NTs (Fig. 7b). The shear localization following this continuous sliding eventually leads to the nucleation of a sub-crack ahead (Fig. 7c). To quantitatively compare the enhanced energy dissipation associated with the zig-zag crack propagation and normal crack (schematically illustrated in Fig. 6), theoretical analysis was performed based on the geometric model illustrated in Fig. 7d, where the main crack is deflected periodically by the secondary NT. Given the average spacing L_{NT} between neighbouring secondary NTs and the crystallographic relation between the secondary NT and sub-crack, the effective zig-zag crack propagation distance and corresponding energy dissipation can be obtained. Two sources of energy dissipation are considered here for zig-zag crack propagation through two neighbouring secondary NTs, *i.e.*, the surface energy for crack opening along the inclined $(1\bar{1}1)$ plane (same as that of the normal crack) and TB sliding along the secondary NT. The total energy $E_{\text{zig-zag}}$ (per specimen thickness) can be expressed as:

$$E_{\text{zig-zag}}=2\gamma_{\text{surface}}\cdot f\cdot L_{\text{NT}}+\gamma_{\text{shear}}h\mathrm{d}h$$

where γ_{surface} and γ_{shear} are the surface energy and TB sliding energy evaluated from MD

simulations, L_{NT} is the spacing between neighboring NTs, h is the length of the initial TB sliding region, dh is the incremental sliding distance along the TB; f is a function of geometric parameters, $f=\sin\alpha / \sin\beta \sin(\theta+\alpha)$, where α =70.5° denotes the orientation of secondary NTs; β and θ denote the orientation of the inclined crack surface inside the specimen (schematically shown in Fig. 7d). Following this geometrical analysis, the incremental energy (per specimen thickness) associated with crack opening is estimated to be $6.57L_{TB}$ (J/m) and the TB sliding energy is estimated to be $1.45nh$ (J/m), where n is the estimated number of full dislocations associated with TB sliding process ($b=a/2[110]$, a=3.53 Å, giving rise to a sliding distance of 0.25 nm for each full dislocation). According to our experimental characterization (Fig. 7b), h is estimated to be $0.52L_{TB}$, and the incremental sliding distance dh is estimated to be a few nanometers prior to the activation of inclined slip, which corresponds to a cumulative slip of n~10 full dislocations. The dissipated energy associated with TB sliding is thus comparable with the energy dissipation of crack opening, rationalizing the nearly doubled CTOD/L ratio for zig-zag crack measured in experiment. It should be noted that extensive dislocation activities and further TB sliding will accommodate the local mechanical thinning and sub-crack formation process, contributing to additional energy dissipation. (Supplementary Notes).

4. Discussion

4.1 General implication of the zig-zag crack

Combining in situ microscale fracture tests performed in TEM, MD simulations, and theoretical analysis, we have unveiled a unique interaction between a propagating crack and a coherent TB in CoCrFeNi MPEA, which draws upon some of the atomistic insights into nucleation mechanism of secondary NTs from inherently defective TBs in our previous work [26]. In situ TEM fracture tests and atomistic characterizations confirm that the secondary NTs can effectively modulate the crack path in the vicinity of a primary TB through a sliding and

opening mechanism (Figs. 2 and 4), leading to zig-zag crack propagation. MD simulations and theoretical analysis quantify energy dissipation associated with such zig-zag crack propagation, which correlates with the sliding distance along secondary NTs as well as the number of periodic crack deflections (Figs. 5–6). These findings not only establish a microscopic zig-zag crack model induced by secondary NTs, but also represent an important step forward for clarifying the underlying relation between the characteristic high fracture toughness and abundant twins in FCC MPEA, which has eluded hitherto systematic experimental analysis in conventional tests. The zig-zag cracking elaborated in this work relies on the coordinated activation of secondary NTs and inclined sub-cracks, underscoring the indispensable role of inherently defective coherent TBs in this toughening mechanism.

Beyond the CoCrFeNi MPEA examined in this work, the zig-zag crack induced by inherently defective TBs are likely to occur in other FCC alloys with low SFE as well. Theoretically, deformation twinning can be preferentially activated with low SFE ranging in 15–45 mJ/m^2 (whereas ultralow SFE may instead induce displacive phase transformation), according to the empirical correlation between SFE and dominant deformation mechanisms in representative FCC alloys [39]. With inherent defects such as steps on the TBs [27, 40], deformation twinning can be further facilitated through the nucleation of secondary NTs from the interfacial sources [26]. The inherently defective TBs and the featured secondary or hierarchical NT structures have been reported in a wide range of FCC metals and alloys, such as Ag [28], stainless steel [24], and Cu-Al alloy [41]. The hierarchical twin structures can effectively blunt and deflect cracks through the TB-crack interaction model proposed in this work (Fig. 6), leading to TB-modulated fracture behaviours similar to those observed in the CoCrFeNi MPEA. Given the dependence of this interaction mechanism on the density and size of intrinsic defects in the TBs, the processing or prior history of alloys [42] can have significant influences on TB-modulated fracture. In this regard, controlling the distribution of atomic-scale

defects in TBs offers an opportunity to modulate fracture behaviors of FCC alloys through dynamic microstructural evolution during external loading.

Nevertheless, we are aware that cracks in thin film samples can exhibit certain different behaviors from their bulk counterpart, such as alternate crack blunting and cleavage reported in the otherwise inherently brittle refractory metal [43]. In this work, the experimental set-up and atomistic simulation models are designed to resemble standard fracture tests with low out-of-plane constraint for the investigation of fracture behaviours of ductile materials (*e.g.*, on Al sheet [44]). The fabricated specimens containing an individual TB and controlled crack activation serve as an ideal platform to study the TB-crack interactions. It remains to be clarified whether the TB-crack interaction and the consequent zig-zag fracture behaviour elaborated with in situ TEM are limited to thin film specimens.

4.2 Comprehensive map of TB-modulated fracture

The above results regarding zig-zag crack not only provide a mechanistic understanding of the TB-modulated fracture behavior of MPEA, but also hold implications for enhancing the fracture resistance of a broad class of ductile FCC alloys with low SFE. To establish a comprehensive understanding of TB-modulated fracture in ductile FCC alloys, we first consider potential cracks along {111} close-packed planes (schematically shown by the double Thompson tetrahedron in Fig. 8a), where the TB-crack interactions in FCC metals/alloys mainly consist of three representative categories. When initiated at the TB (plane ACB in Fig. 8b), the crack is prone to propagating along the TB as typical mode I crack [37, 45]. In this case, the crack propagation resistance depends on the intrinsic strength of coherent TB. However, crack propagation along the coherent TB can be rather sluggish in ductile metals or alloys, due to both the intrinsic stability of coherent TB (compared with that of general HAGBs) and the vast availability of other plastic deformation mechanisms ahead of the crack tip, such

as dislocation emission [40, 45]. In contrast, when the crack lies along the other edge-on plane (BCD in Fig. 8c) and propagates towards to the TB (*i.e.*, hard mode), slip transmission following the crack deflection occurs preferentially. With increasing TB density, such as nanotwinned metals [30, 31, 46], consecutive deflection can significantly enhance the crack resistance with reduced TB spacing (schematically shown in Fig. 8c). However, at extreme TB spacing (*i.e.*, several atomic layers), direct slip transmission along the (001) non-close-packed plane can be triggered [47], and the crack can potentially penetrate the nanotwins ahead. In addition to these two classic categories of TB-crack interactions, our work elaborates a third interaction mode involving TB and inclined crack plane (ACD or ABD), which indicates that coherent TBs can also blunt the cracks nearby, even when the initial crack adopts a deviating path from the TB. Essentially, the inherently defective TBs prove to modulate the crack propagation path in the vicinity of a primary TB through the activation of secondary or even hierarchical NTs, leading to zig-zag crack propagation (schematically shown in Fig. 8d). This mechanism can be activated within a range of TB orientations (Fig. 4a–c), given the preferential activation of secondary or hierarchical NTs from the TB defects. According to our zig-zag crack model (Fig. 7d), the energy dissipation associated with TB sliding is comparable to crack opening. Thus, the overall effective crack propagation distance arising from both crack opening and TB sliding is nearly doubled compared with a normal crack along {111} planes in SC lattices.

Combining these three categories of TB-crack interactions in the context of {111} close-packed planes, a comprehensive map of TB-modulated fracture can be established, which holds general implications for FCC alloys. Meanwhile, we note that initial crack can also be activated on other lattice planes, especially under the complex stress condition ahead of the crack tip. For example, crack propagation almost parallel to the (001) plane in MPEA has been reported in both modelling [48] and experiments [14]. In these cases, the crack propagation is mainly

facilitated by void formation coordinated with twinning-dominated plasticity within the ligaments between the neighboring voids at the final deformation stage of ductile alloy. The three representative mechanisms within this comprehensive map (Figs. 8b–d), as well as other potential crack on non-close-packed planes, collectively contribute to the TB-modulated fracture within individual grains, which marks an important step to quantitatively correlate the abundant twins with the overall enhanced fracture toughness in FCC alloys.

Although the current model mainly elaborates the interactions between a propagating crack and an individual TB (Fig. 8b–d), it suggests an approach to quantitatively correlate the abundant deformation twins with the overall enhanced fracture toughness in FCC alloys. When we extend the NT nucleation model from inherently defective TBs to general GBs, which are also preferential nucleation sites of lattice defects [11, 49], zig-zag crack via consecutive sliding and sub-crack nucleation along NTs are expected to occur more frequently within these grains, depending on the crystallographic relations and the density of NTs ahead of the crack tip. Further taking into consideration the plastic anisotropy among different grains, this comprehensive theory for each individual TB-crack interaction can be potentially generalized for TB-modulated transgranular fracture in polycrystalline alloys. Future works are required to precisely determine the TB-modulated fracture toughness in polycrystalline materials, which can inspire further multi-scale modelling and eventually guide the structural design of alloy for enhanced damage tolerance.

5. Conclusions

Combining in situ TEM microscale fracture test of CoCrFeNi MPEA, MD simulation, and theoretical analysis, we have unveiled a microscopic mechanism of the interaction between cracks and coherent TBs, which is of general importance to understanding TB-modulated

fracture behaviors in FCC MPEAs and their characteristic high toughness. The following conclusions can be drawn from this study:

(1) The steps on the inherently defective TBs can facilitate the activation of secondary NTs in CoCrFeNi MPEA. Through this mechanism, cracks nearby can be effectively blunted through consecutive sliding along secondary NT and nucleation of sub-crack ahead, leading to zig-zag crack propagation in the vicinity of a primary TB.

(2) A geometric model has been developed to quantify the enhanced fracture resistance associated with the zig-zag crack propagation in MPEA, which indicates nearly doubled energy dissipation compared with that of a normal crack.

(3) The deformation twin mediated consecutive sliding-opening crack propagation mechanisms can help bridge the current gap between increasing recognition of hierarchical twin configurations and enhanced toughness in MPEA. Thus, these findings potentially contribute to a more comprehensive understanding of TB-modulated damage tolerance in FCC alloys with low SFE.

References

[1] B. Cantor, I.T.H. Chang, P. Knight, A.J.B. Vincent, Microstructural development in equiatomic multicomponent alloys, Mater. Sci. Engin. A 375-377 (2004) 213-218.

[2] Z. Li, K.G. Pradeep, Y. Deng, D. Raabe, C.C. Tasan, Metastable high-entropy dual-phase alloys overcome the strength–ductility trade-off, Nature 534(7606) (2016) 227-230.

[3] Q. Ding, Y. Zhang, X. Chen, X. Fu, D. Chen, S. Chen, L. Gu, F. Wei, H. Bei, Y. Gao, M. Wen, J. Li, Z. Zhang, T. Zhu, R.O. Ritchie, Q. Yu, Tuning element distribution, structure and properties by composition in high-entropy alloys, Nature 574(7777) (2019) 223-227.

[4] H. Luo, S.S. Sohn, W. Lu, L. Li, X. Li, C.K. Soundararajan, W. Krieger, Z. Li, D. Raabe, A strong and ductile medium-entropy alloy resists hydrogen embrittlement and corrosion, Nat. Commun. 11(1) (2020) 3081.

[5] Y. Zhao, D.-H. Lee, M.-Y. Seok, J.-A. Lee, M.P. Phaniraj, J.-Y. Suh, H.-Y. Ha, J.-Y. Kim, U. Ramamurty, J.-i. Jang, Resistance of CoCrFeMnNi high-entropy alloy to gaseous hydrogen embrittlement, Scr. Mater. 135 (2017) 54-58.

[6] B. Gludovatz, A. Hohenwarter, D. Catoor, E.H. Chang, E.P. George, R.O. Ritchie, A fracture-resistant high-entropy alloy for cryogenic applications, Science 345(6201) (2014) 1153-1158.

[7] F. Otto, A. Dlouhý, C. Somsen, H. Bei, G. Eggeler, E.P. George, The influences of temperature and microstructure on the tensile properties of a CoCrFeMnNi high-entropy

alloy, Acta Mater. 61(15) (2013) 5743-5755.
[8] Y. Zhao, J.-M. Park, J.-i. Jang, U. Ramamurty, Bimodality of incipient plastic strength in face-centered cubic high-entropy alloys, Acta Mater. 202 (2021) 124-134.
[9] P. Wu, K. Gan, D. Yan, Z. Fu, Z. Li, A non-equiatomic FeNiCoCr high-entropy alloy with excellent anti-corrosion performance and strength-ductility synergy, Corros. Sci. 183 (2021) 109341.
[10] K. Lu, A. Chauhan, D. Litvinov, M. Schneider, G. Laplanche, J. Aktaa, Cooperative deformation mechanisms in a fatigued CoCrNi multi-principal element alloy: A case of low stacking fault energy, J. Mech. Phys. Solids 180 (2023).
[11] G. Laplanche, A. Kostka, C. Reinhart, J. Hunfeld, G. Eggeler, E.P. George, Reasons for the superior mechanical properties of medium-entropy CrCoNi compared to high-entropy CrMnFeCoNi, Acta Mater. 128 (2017) 292-303.
[12] P. Kumar, M. Michalek, D.H. Cook, H. Sheng, K.B. Lau, P. Wang, M. Zhang, A.M. Minor, U. Ramamurty, R.O. Ritchie, On the strength and fracture toughness of an additive manufactured CrCoNi medium-entropy alloy, Acta Mater. 258 (2023).
[13] B. Gludovatz, A. Hohenwarter, K.V. Thurston, H. Bei, Z. Wu, E.P. George, R.O. Ritchie, Exceptional damage-tolerance of a medium-entropy alloy CrCoNi at cryogenic temperatures, Nat. Commun. 7 (2016) 10602.
[14] Z.J. Zhang, M.M. Mao, J. Wang, B. Gludovatz, Z. Zhang, S.X. Mao, E.P. George, Q. Yu, R.O. Ritchie, Nanoscale origins of the damage tolerance of the high-entropy alloy CrMnFeCoNi, Nat. Commun. 6 (2015) 10143.
[15] Q. Zhang, R. Niu, Y. Liu, J. Jiang, F. Xu, X. Zhang, J.M. Cairney, X. An, X. Liao, H. Gao, X. Li, Room-temperature super-elongation in high-entropy alloy nanopillars, Nat. Commun. 14(1) (2023) 7469.
[16] W. Li, D. Xie, D. Li, Y. Zhang, Y. Gao, P.K. Liaw, Mechanical behavior of high-entropy alloys, Prog. Mater Sci. 118 (2021).
[17] M. Schneider, J. P. Couzinié, A. Shalabi, F. Ibrahimkhel, A. Ferrari, F. Körmann, G. Laplanche, Effect of stacking fault energy on the thickness and density of annealing twins in recrystallized FCC medium and high-entropy alloys, Scr. Mater. 240 (2024).
[18] Z. Zhang, H. Sheng, Z. Wang, B. Gludovatz, Z. Zhang, E.P. George, Q. Yu, S.X. Mao, R.O. Ritchie, Dislocation mechanisms and 3D twin architectures generate exceptional strength-ductility-toughness combination in CrCoNi medium-entropy alloy, Nat. Commun. 8 (2017) 14390.
[19] S. Wei, Y. Zhao, J.-i. Jang, U. Ramamurty, Rate-dependent mechanical behavior of single-, bi-, twinned-, and poly-crystals of CoCrFeNi high-entropy alloy, J. Mater. Sci. Technol. 120 (2022) 253-264.
[20] R.O. Ritchie, The conflicts between strength and toughness, Nat. Mater. 10 (2011) 817-22.
[21] Z. Zhang, Z. Jiang, Y. Xie, S.L.I. Chan, J. Liang, J. Wang, Multiple deformation mechanisms induced by pre-twinning in CoCrFeNi high entropy alloy, Scr. Mater. 207 (2022).
[22] Y. Wang, B. Liu, K. Yan, M. Wang, S. Kabra, Y.-L. Chiu, D. Dye, P.D. Lee, Y. Liu, B. Cai, Probing deformation mechanisms of a FeCoCrNi high-entropy alloy at 293 and 77 K using in situ neutron diffraction, Acta Mater. 154 (2018) 79-89.
[23] T. Cao, Q. Zhang, L. Wang, L. Wang, Y. Xiao, J. Yao, H. Liu, Y. Ren, J. Liang, Y. Xue, X. Li, Dynamic deformation behaviors and mechanisms of CoCrFeNi high-entropy alloys, Acta Mater. 260 (2023).
[24] A.Y. Chen, L.L. Zhu, L.G. Sun, J.B. Liu, H.T. Wang, X.Y. Wang, J.H. Yang, J. Lu, Scale law of complex deformation transitions of nanotwins in stainless steel, Nat. Commun. 10(1) (2019) 1403.

[25] Z. Kou, R. Huang, Y. Yang, T. Feng, S. Tang, S. Lan, L. Yang, Revealing the atomic-scale evolution of sessile disconnections on twin boundaries during deformation, Scr. Mater. 221 (2022) 114956.
[26] Q. Zhu, Q. Huang, Y. Tian, S. Zhao, Y. Chen, G. Cao, K. Song, Y. Zhou, W. Yang, Z. Zhang, X. An, H. Zhou, J. Wang, Hierarchical twinning governed by defective twin boundary in metallic materials, Sci. Adv. 8 (2022) eabn8299.
[27] Y.M. Wang, F. Sansoz, T. LaGrange, R.T. Ott, J. Marian, T.W. Barbee, A.V. Hamza, Defective twin boundaries in nanotwinned metals, Nature Materials 12(8) (2013) 697-702.
[28] X. Liu, L. Sun, L. Zhu, J. Liu, K. Lu, J. Lu, High-order hierarchical nanotwins with superior strength and ductility, Acta Mater. 149 (2018) 397-406.
[29] W.P. Li, X.G. Wang, B. Liu, Q.H. Fang, C. Jiang, Fracture mechanisms of a Mo alloyed CoCrFeNi high entropy alloy: In-situ SEM investigation, Mater. Sci. Engin. A 723 (2018) 79-88.
[30] S.-W. Kim, X. Li, H. Gao, S. Kumar, In situ observations of crack arrest and bridging by nanoscale twins in copper thin films, Acta Mater. 60 (2012) 2959-2972.
[31] Z. Zeng, X. Li, L. Lu, T. Zhu, Fracture in a thin film of nanotwinned copper, Acta Mater. 98 (2015) 313-317.
[32] A. Neogi, R. Janisch, Twin-boundary assisted crack tip plasticity and toughening in lamellar γ-TiAl, Acta Mater. 213 (2021).
[33] Y. Zhang, Y. Bu, X. Fang, H. Wang, A compact design of four-degree-of-freedom transmission electron microscope holder for quasi-four-dimensional characterization, Science China Technological Sciences 63 (2020) 1272-1279.
[34] S. Plimpton, Fast Parallel Algorithms for Short-Range Molecular Dynamics, J. Comput. Phys. 117(1) (1995) 1-19.
[35] O.R. Deluigi, R.C. Pasianot, F.J. Valencia, A. Caro, D. Farkas, E.M. Bringa, Simulations of primary damage in a High Entropy Alloy: Probing enhanced radiation resistance, Acta Mater. 213 (2021).
[36] S. Alexander, Visualization and analysis of atomistic simulation data with OVITO–the Open Visualization Tool, Modell. Simul. Mater. Sci. Eng. 18 (2010) 015012.
[37] Q. Zhu, L. Kong, H. Lu, Q. Huang, Y. Chen, Y. Liu, W. Yang, Z. Zhang, F. Sansoz, H. Zhou, J. Wang, Revealing extreme twin-boundary shear deformability in metallic nanocrystals, Sci. Adv. 7 (2021) eabe4758.
[38] Y. Yue, Q. Zhang, X. Zhang, Z. Yang, P. Yin, L. Guo, In Situ Observation of Twin Boundary Sliding in Single Crystalline Cu Nanowires, Small 13 (2017) 1604296.
[39] B.C. De Cooman, Y. Estrin, S.K. Kim, Twinning-induced plasticity (TWIP) steels, Acta Mater. 142 (2018) 283-362.
[40] L.E. Murr, Dislocation Ledge Sources: Dispelling the Myth of Frank–Read Source Importance, Metall. Mater. Trans. A 47 (2016) 5811-5826.
[41] X.H. An, S.D. Wu, Z.G. Wang, Z.F. Zhang, Significance of stacking fault energy in bulk nanostructured materials: Insights from Cu and its binary alloys as model systems, Prog. Mater Sci. 101 (2019) 1-45.
[42] M. Dao, L. Lu, Y.F. Shen, S. Suresh, Strength, strain-rate sensitivity and ductility of copper with nanoscale twins, Acta Mater. 54 (2006) 5421-5432.
[43] Y. Lu, Y. Chen, Y. Zeng, Y. Zhang, D. Kong, X. Li, T. Zhu, X. Li, S. Mao, Z. Zhang, L. Wang, X. Han, Nanoscale ductile fracture and associated atomistic mechanisms in a body-centered cubic refractory metal, Nat. Commun. 14(1) (2023) 5540.
[44] J. Heerens, M. Schödel, Characterization of stable crack extension in aluminium sheet material using the crack tip opening angle determined optically and by the δ5 clip gauge technique, Engin. Fract. Mech. 76(1) (2009) 101-113.
[45] Y. Cheng, Z.H. Jin, Y.W. Zhang, H. Gao, On intrinsic brittleness and ductility of

intergranular fracture along symmetrical tilt grain boundaries in copper, Acta Mater. 58 (2010) 2293-2299.
[46] Z.W. Shan, L. Lu, A.M. Minor, E.A. Stach, S.X. Mao, The effect of twin plane spacing on the deformation of copper containing a high density of growth twins, JOM 60 (2008) 71-74.
[47] J. Wang, G. Cao, Z. Zhang, F. Sansoz, Size-dependent dislocation–twin interactions, Nanoscale 11 (2019) 12672-12679.
[48] W. Zhong, S. Hayakawa, H. Xu, K. An, A.Y. Borisevich, J.L. Cicotte, E.P. George, Y. Yang, Decipher multiple deformation mechanisms in a FeCrCoNi medium entropy alloy for sustained work hardening, Int. J. Plast. (2023).
[49] V. Yamakov, D. Wolf, S.R. Phillpot, A.K. Mukherjee, H. Gleiter, Dislocation processes in the deformation of nanocrystalline aluminium by molecular-dynamics simulation, Nat. Mater. 1 (2002) 45-48.

Acknowledgement

This research has been supported by A*STAR under its Advanced Models for Additive Manufacturing (AM^2) programme (Award M22L2b0111). Q.Z. and H.G. acknowledge Nanyang Technological University for support of this work through a Distinguished University Professorship for H.G. Q.Z. would like to acknowledge the Facility for Analysis, Characterisation, Testing and Simulation (FACTS), Nanyang Technological University, Singapore, for use of their FIB and TEM. The computational work for this article was performed on resources of the National Supercomputing Centre (NSCC), Singapore (https://www.nscc.sg).

Author contributions:

H.G. and Q.Z. designed the project. Q.Z. conducted the experiments. Z.L. performed the simulations. Q.Z., Z.L., S.W., Y.Z. and J.W. analyzed the data. Q.Z., Z.L. and H.G. wrote the paper. S.W., Y.Z., U.R. and J.W. contributed to paper revision.

Competing interests:

The authors declare no competing interests.

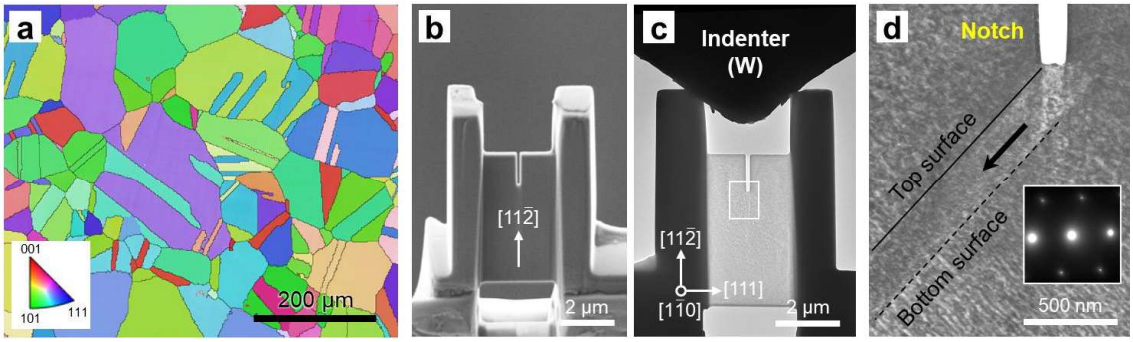

Figure 1. Site-selective specimen fabrication and in situ microscale fracture test in TEM. (a) Grain morphology of the as-received CoCrFeNi equiatomic MPEA superimposed by orientation map, which contains large number of Σ3 coherent TBs. (b) SEM image of a selectively FIB-fabricated specimen. (c) In situ microscale fracture test in TEM. (d) Preferential activation of an inclined (1$\bar{1}$1) slip from the pre-set notch in the [11$\bar{2}$]-aligned specimen (confirmed by the inset SAED pattern). Subsequent shear localization leads to the nucleation of a sharp crack along this inclined slip plane (indicated by the black arrow).

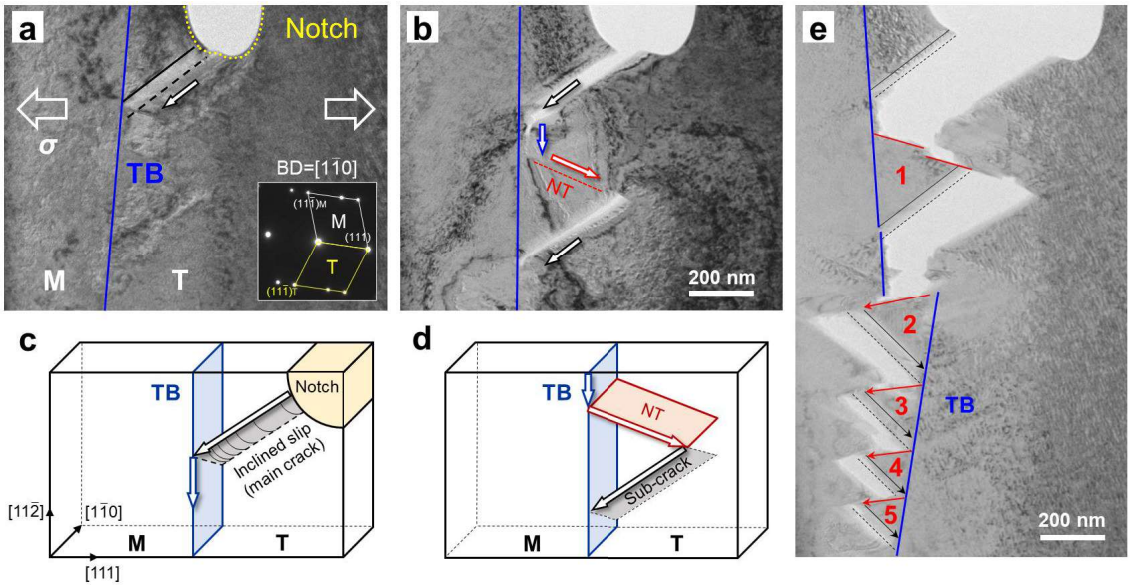

Figure 2. Microscopic zig-zag crack propagation in the vicinity of a pre-existing coherent TB. (a) Activation of a main crack along an inclined slip plane (delineated by the black lines) towards the pre-existing coherent TB (blue line). The inset SAED pattern confirms the presence of a pre-existing TB in the specimen. (b) Consecutive deflections of the crack in the vicinity of TB. The black, blue, and red arrows indicate the consecutive crack propagation along the inclined slip plane, primary TB and secondary NT, respectively. (c–d) Schematic illustrate the crack propagation path in (a) and (b), respectively. (e) Consecutive zig-zag crack propagation in the vicinity of the primary TB.

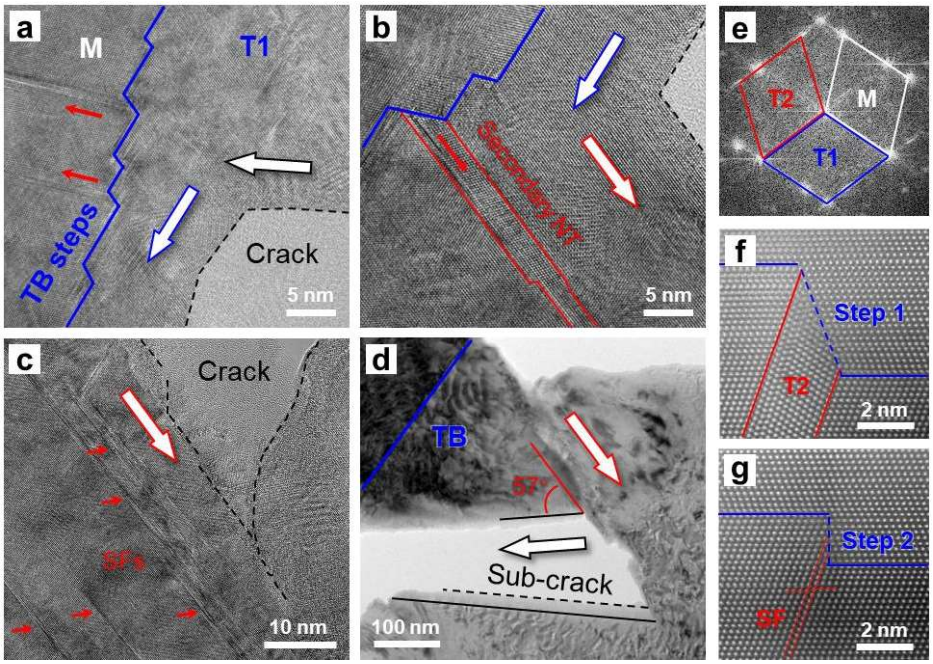

Figure 3. Microstructural origin associated with the zig-zag crack propagation along the primary TB. (a) Atomic structure of the TB at the first crack deflection site. (b) TB crack deflected by a secondary NT ahead. (c) Crack propagation accompanied by lattice sliding after deflection by the secondary NT. (d) Reactivation of inclined slip and the formation of a sub-crack (indicated by the black arrow). (e) Fast Fourier transform (FFT) pattern of the hierarchical twin structures in (b). (f–g) Atomic structures of the neighboring steps in the primary TB associated with the nucleation of a secondary NT (f) and a SF (g).

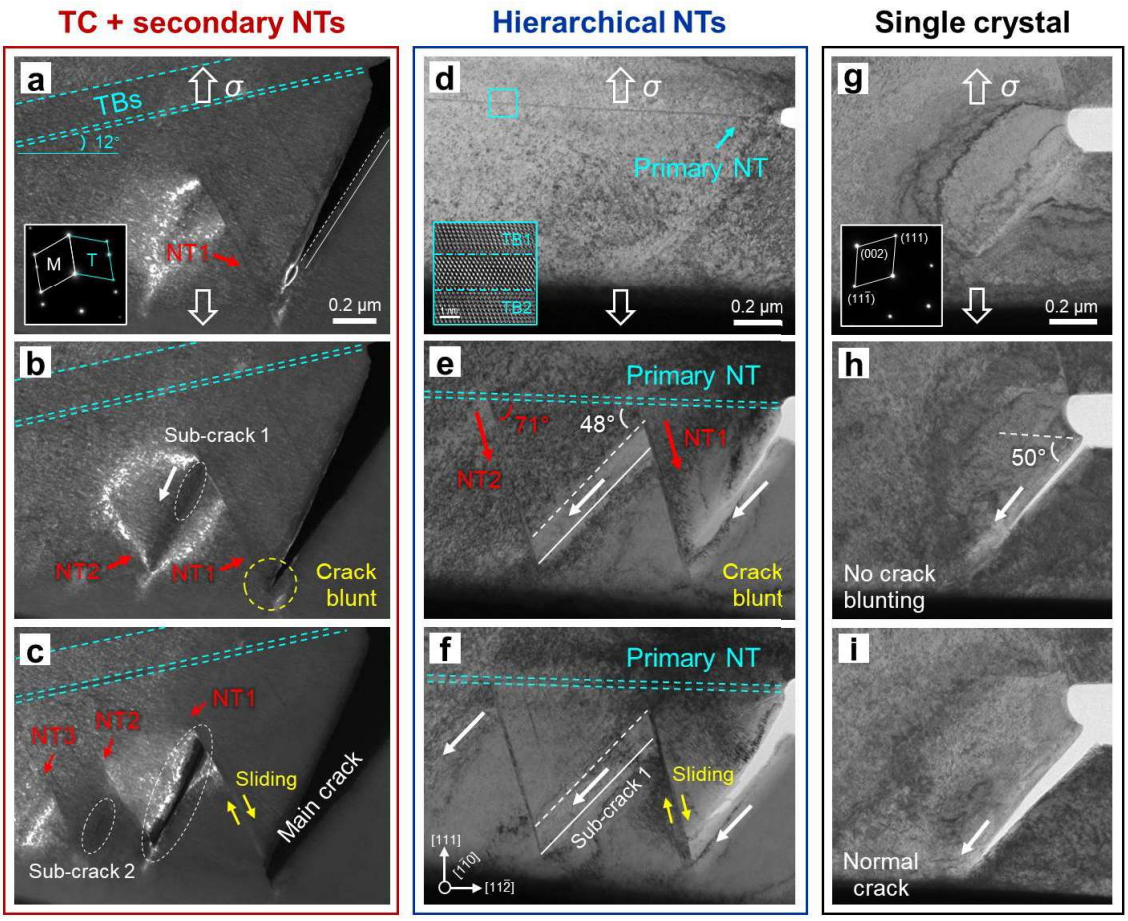

Figure 4. **TB-induced zig-zag propagation of a deviating crack in CoCrFeNi MPEA.** (a-c) Dark-field TEM snapshots showing the zig-zag crack propagation in the vicinity of slanted TBs. (a) The deviating crack blunted by the secondary NT (indicated by the red arrow) generated from the primary TB. (b-c) Consecutive blunting and sub-crack nucleation leads to zig-zag crack. (d-f) Zig-zag crack along the hierarchical NT configurations. (d) CoCrFeNi specimen containing of a nanotwin (inset HRTEM image) along the indentation direction. (d-f) Zig-zag crack induced by secondary NTs. (g–i) Normal crack along the inclined (1$\bar{1}$1) plane in single crystal without evident blunting.

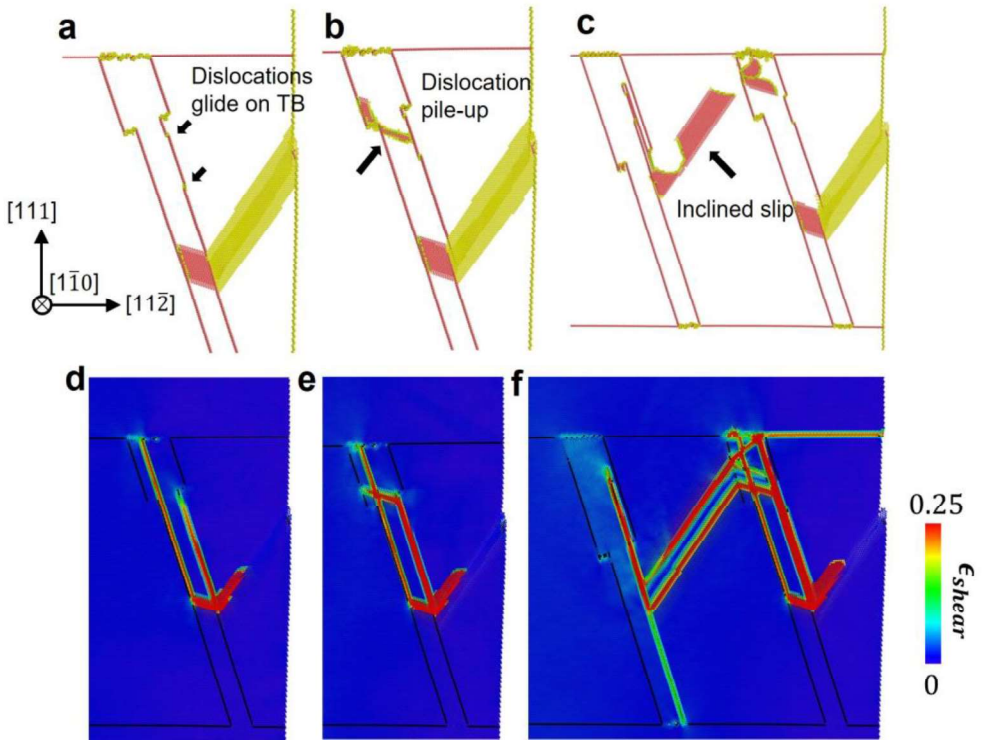

Figure 5. Atomistic mechanisms of the TB-crack interaction underlying the zig-zag crack propagation in CoCrFeNi MPEA. (a) Dislocation pairs emitted from the main crack and glide along the secondary NT under tensile loading. (b) Nucleation of Shockley partials from the intersection site on the secondary NT. (c) Re-activation of inclined slip between the secondary NTs. FCC atoms are removed for clear demonstration of TBs and crack. Red and yellow atoms indicate HCP and unknown coordination structure respectively, while green lines represent the Shockley partials. (d–f) Atomistic mapping of von Mises strain in (a–c). Atoms on TBs are colored black for reference.

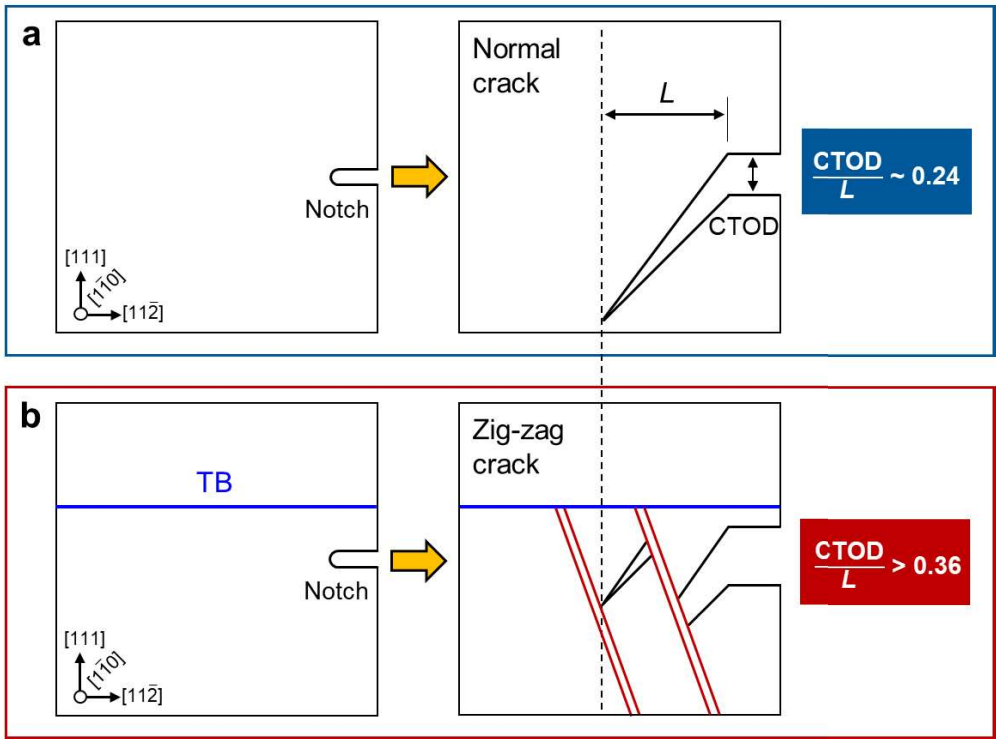

Figure 6. Enhanced fracture resistance associated with TB-modulated zig-zag crack propagation. (a–b) Schematics of a normal crack (a) and zig-zag crack (b) during the microscale fracture test of [112]-aligned SC and TC specimens. The fracture resistance is characterized by the ratio between crack tip opening displacement (CTOD) and crack propagation distance L in both cases.

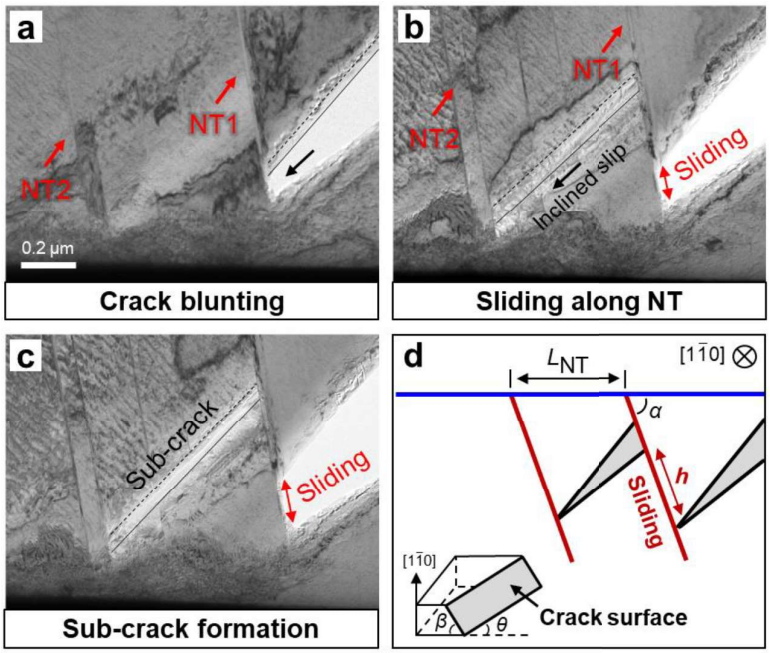

Figure 7. Sub-crack nucleation and energy dissipation associated with sliding along NTs. (a) Blunting of the main crack by NT1. (b–c) Nucleation of sub-crack following the inclined slip between NT1 and NT2, which is accompanied by sliding along the secondary NT. (d) Schematic model of the microscopically zig-zag crack for quantitative analysis of energy dissipation.

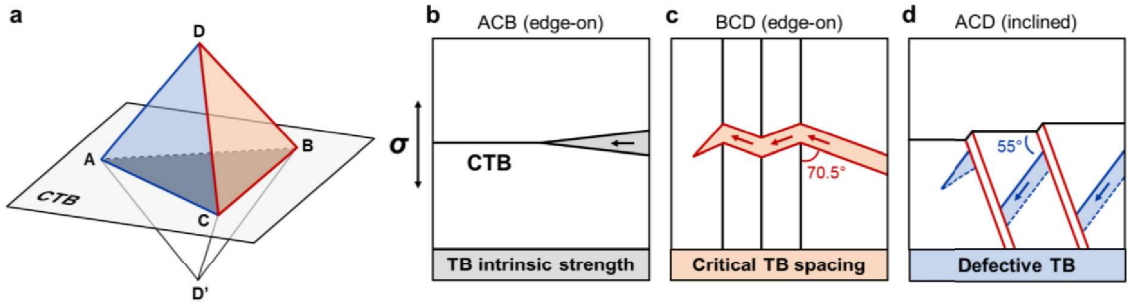

Figure 8. Representative mechanisms of TB-modulated fracture in FCC metals with low SFE. (a) Thompson tetrahedron showing the orientation relations between CTB and all potential cracks along {111} close-packed planes (colored grey, red and blue) in FCC metals. (b–d) Schematics of different crack propagation modes modulated by coherent TB.

Table 1. CTOD/*L* ratio measured from in situ experiments.

Specimen	CTOD (nm)	*L* (nm)	CTOD/*L*	Snapshots
Norm-1	127	593	0.21	
Norm-2	190	810	0.23	
Norm-3	157	559	0.28	Fig. 4i
Norm-4	200	789	0.25	
Zig-zag 1	76	173	0.36	Fig. 4f
Zig-zag 2	600	1610	0.37	Fig. 2e
Zig-zag 3	426	879	0.48	Fig. 4c